crystals

MDPI

Article

Gemological and Mineralogical Characteristics of Emerald from Ethiopia

Zixuan Huang [1], Geng Li [1,*], Liqun Weng [2] and Meilun Zhang [1]

[1] School of Gemology, China University of Geosciences, Beijing 100083, China
[2] National Jewelry Testing Center (Guangdong) Co., Ltd., Guangzhou 511483, China
* Correspondence: ligeng@cugb.edu.cn

Abstract: Ethiopia has been gaining attention in recent years as an emerging source of high-quality emerald. Ethiopian emerald samples with different colors ranging from dark green to light green were selected to study the gemological properties, chemical composition, and spectral characteristics. The Ethiopian emeralds were examined using conventional gemological instruments, including X-ray fluorescence spectrometry, LA-ICP-MS, UV/Vis/NIR, infrared spectrometry, and Raman spectrometry, providing a wealth of data and research information related to Ethiopian emeralds. The EDXRF results show that the chemical composition of Ethiopian emeralds is distinctly regional compared to emeralds of Colombian origin, being low in Cr, low in V, and high in Fe. LA-ICP-MS results demonstrate consistent results for Cr (734.34 to 1644.3 ppmw), V (89.61 to 106.61 ppmw), and Fe (4468.04 to 5022.3 ppmw) based on the chemical composition analysis by EDXRF. In addition, the LA-ICP-MS assay revealed that the combination of alkali metals (Li, Na, K, Rb, and Cs) and some trace elements (Sc, V, Cr, and Fe) could distinguish the Ethiopian emeralds from those from other regions. The Ethiopian emerald had absorption of Fe^{2+}, Cr^{3+}, V^{3+}, and Fe^{3+}, and the typical absorption intensity of Fe^{2+} (around 850 nm) was higher than that of Fe^{3+} (around 371 nm) in the UV/Vis/NIR spectra. The infrared spectrum of samples indicated that the absorption of type II H_2O was higher than type I H_2O in the emeralds from Ethiopia, which is consistent with the high content of alkali metals detected by LA-ICP-MS that would lead to an increase in the content of type II H_2O. The Raman spectra showed absorption at 410 cm^{-1}, 569 cm^{-1}, 687 cm^{-1}, 995 cm^{-1}, and 1067 cm^{-1}, with an emerald species recognition pattern. The gas–liquid two-phase inclusions of the emerald in this area were mainly CO_2 and H_2O, and the samples contained typical dark inclusions of magnesium-rich biotite sheets that revealed the tectonic-magmatic-related geological environment in this region.

Keywords: emerald from Ethiopia; gemological and mineralogical characteristics; spectroscopy

check for updates

Citation: Huang, Z.; Li, G.; Weng, L.; Zhang, M. Gemological and Mineralogical Characteristics of Emerald from Ethiopia. *Crystals* **2023**, *13*, 233. https://doi.org/10.3390/cryst13020233

Academic Editor: Sergey V. Krivovichev

Received: 19 December 2022
Revised: 24 January 2023
Accepted: 26 January 2023
Published: 29 January 2023

Copyright: © 2023 by the authors. Licensee MDPI, Basel, Switzerland. This article is an open access article distributed under the terms and conditions of the Creative Commons Attribution (CC BY) license (https://creativecommons.org/licenses/by/4.0/).

1. Introduction

Emerald is the bluish-green to green to a yellowish-green variety of beryl (with a formula of $Be_3Al_2[Si_6O_{18}]$), which has been one of the most sought-after gems for several centuries [1]. Emerald is rare, precious, and difficult to mine [2,3]. The study of the characteristics of emeralds is of great significance, as it provides clues for the relevant geological evolution process and economic value [4,5].

Gemologists have studied the gemological characteristics of emeralds of different origin, describing how they appear under conventional gemological instruments [6–9], as well as the inclusions of emeralds, including two- and three-phase fluid inclusions as well as solid inclusions [7,10]. Inclusions are an important basis for indicating geological origin, and research on emerald origin and its metallogenic geology is plentiful [11–13]. Primary emerald deposits are subdivided into two types on the basis of their geological environment of formation: tectonic-magmatic-related (type I) and tectonic-metamorphic-related (type II). Several sub-types are defined, especially type IA, which is characterized by the intrusion of

pegmatites or quartz veins in mafic and ultramafic rocks, or M-UMR, accompanied by huge hydrothermal fluid circulation and metasomatism with the formation of emerald-bearing desilicated pegmatite (plumasite) and biotite schist [14], hosted in M-UMR, which accounts for about 70% of worldwide production (Brazil, Zambia, Russia, and others). Type IB in sedimentary rocks and type IC in granitic rocks are of minor importance [14]. Using hydrogen and oxygen isotopes and related components, some studies inferred the formation age and origin of emeralds [15]. In addition to the discussion of geological characteristics, the research around emeralds also focuses on their chromogenic mechanism, with the main color elements of emeralds being Cr, V, and Fe [16–18]. Besides the chromogenic elements, emeralds from some areas are characterized by a high content of alkali metals, whose infrared spectrum shows that the absorption of type II H_2O is stronger than that of type I H_2O [5,9,16].

The mining of emeralds in Ethiopia began in 2010 and is located near the small town of Shakiso, Oromiya Region [2,19–23]. Ethiopia produces fewer gem-grade emerald crystals, and most of the mine area was temporarily closed in 2016, resulting in fewer Ethiopian emeralds appearing on the market [2,19–23]. At present, there are few studies on Ethiopian emeralds, revealing mainly their chemical composition with a high content of alkali metals in this region [19]. There is a lack of systematic studies on their gemological and mineralogical characteristics. Geographic origin determination is getting more complicated, considering that gems can grow in similar geologic environments but in different countries. However, gemmological laboratories are asked to issue reports mentioning a gem's geographical origin [24]. The majority of gem-quality emeralds are found in primary deposits [24]; they contain inclusions that are associated with their geology that might help gemmological laboratories build an accurate database to trace the origin of an unknown sample.

2. Geology

Ethiopia is located in the East African Orogen within the Pan-African Tectonic Belt. The Pan-African Tectonic Belt was formed between 1000 and 450 Ma, and the Ethiopian Basement ranges in age from 880 to 550 Ma [25,26]. This active belt separates West Africa, the Nile, Kalaha Desert, Congo, South Africa, and other stable cratons on the African continent, and it is composed of the Arabian–Nubian Shield and the Mozambique Belt [26–29]. Ethiopia is located in the Nubian Shield, which is mainly composed of Neoproterozoic metamorphic rocks and various intrusive rocks [27,29] (Figure 1).

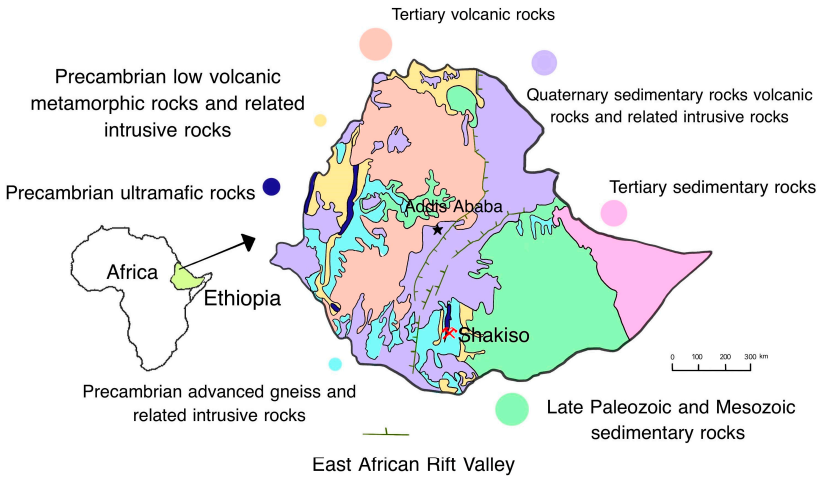


Figure 1. Outline map of the geological structure of Ethiopia. The emerald mining area is indicated by the red marker. Modified from [29].

The southern Ethiopian Precambrian Shield terrain is largely composed of sutured medium- to high-grade assemblages of Precambrian crystalline basement, consisting of

metamorphic complexes and associated plutonic rocks that belong to the northern and southern continuations of the Mozambique belt and the Arabian–Nubian Shield [30]. Brittle–ductile shear zones, folds, and brittle faults are developed in the Precambrian metamorphic rock area where the Ethiopian emerald deposit is located [27–29]. The main lithologies of ductile shear zones are various schists, gneisses, granites, etc. [29]. The Shakiso emeralds occur in the Neoproterozoic Adola Belt of southern Ethiopia [29]. The Adola Belt consists of two lithotectonic terranes: a Granite–Gneiss Complexes (GGCs) terrane and an Ophiolite Fold and Thrust Belts (OFTBs) terrane, which are separated by large faults and shear zones [26]. The East African rift zone generally runs through Ethiopia in the NE direction [25–30]. There are many volcanoes and geological activities on the plateaus on both sides of the rift zone [25–29]. The emplacement of the Kenticha pegmatite was at ca. 530 Ma and temporally related to the post-collisional phase of granitic magmatism at 570–520 Ma, after the last tectonic stage of east African orogeny during the late stage of Gondwana assembly [31]. This age similarity suggests coeval emplacement of the Kenticha field pegmatites, which include the Shakiso pegmatite [31]. Therefore, the emerald crystals mined in Ethiopia include many fractures.

The emerald deposit is located in the southern area, Oromiya Region, which is mainly composed of Precambrian high-grade gneiss, intrusive rocks, and ultramafic rocks [29]. The Kenticha Belt was intruded by a series of peraluminous post-orogenic biotite granites, two-mica granites, and associated pegmatites [2]. Magmatic fractionation and later hydrothermal/metasomatic alteration caused the enrichment/depletion of minerals at different zones of the pegmatite, leading to ore mineralization [27,32]. There are Be-, Li-, Cs-, and Rb-bearing zones of pegmatites, which are structurally controlled [26]. Other rocks surrounding the host rocks include schists and gneisses of varying composition [26].

Locally, the host rocks to the Shakiso and neighboring pegmatites are ultramafic rocks of the Kenticha OFTB, now metamorphosed to serpentinite and talc-tremolite schist [2]. Proximal to the Shakiso mine, the host rock to the emerald pegmatite is dominantly talc schist with minor chlorite [2]. The ultramafic rocks overlap the schist rich in mica and chlorite. It is inferred that ultrabasic rocks are the main rocks for the mineralization of emerald.

3. Materials and Methods

Seven Ethiopian emeralds (numbered E-1 to E-7) were selected for investigation, five of which were faceted (E-1 to E-5) and two were crystals (E-6 and E-7). All samples were acquired by the authors from a local reliable dealer in Shakiso, Ethiopia. The sample color ranged from light green to dark green, with darker samples having a slightly blue tone. Images of the samples are shown in Figure 2. All experiments in this paper were completed at the National Jewelry Testing Center (Guangzhou), China, except for LA-ICP-MS.

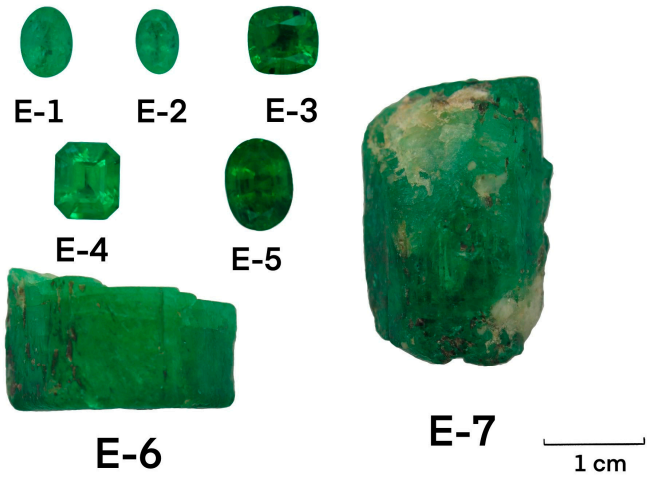


Figure 2. Ethiopian emerald samples (weight ranging from 0.113 to 23.913 g) in this study.

The Ethiopian emerald samples were observed using an ultra-depth microscope, energy-dispersive X-ray fluorescence spectrometer (EDXRF), LA-ICP-MS, UV/Vis/NIR spectrometer, infrared spectrometer, and Raman spectrometer.

The ultra-depth microscope model was a KEYENCE VHX-5000 (Osaka, Japan), with a magnification of 20× to 200×.

The model of the polarized energy-dispersive X-ray fluorescence spectrometer experimental instrument was a Shimadzu X-ray EDX7000 (Kyoto, Japan), which is used for nondestructive testing and allows semi-quantitative analysis. The range of test elements is ^{13}Al to ^{92}U, the working voltage is 220 V, the diameter of the collimator is 1 to 3 mm, and the test environment is a non-vacuum atmosphere.

The analysis of trace elements in emeralds was completed at the LA-ICP-MS Laboratory, National Geological Experiment and Test Center. Laser ablation inductively coupled plasma mass spectrometry (LA-ICP-(SF)MS) analysis equipment consisted of a New Wave UP213 laser denudation system and a Thermo-Finnigan Element II high-resolution fan-field mass spectrometer. The laser ablation system uses He as the ablation material to transport the carrier gas. The laser spot beam diameter is 35 μm, the frequency is 10 Hz, and the laser energy density is about 12 J/cm^2. ICP-MS analysis uses a low-resolution mode to detect 50 major and trace elements/isotopes in single mineral samples, ranging from ^{7}Li to ^{238}U. Each mass peak was analyzed with 10 points of data, and each point analysis time was 2 ms. Before analysis, the denudation NIST612 was tuned to make the denudation signal of ^{139}La and ^{232}Th (35.8 and 37.8ppm, respectively) greater than 2×10^5 cps (counts per second), and the yield of ThO^+/Th^+ oxidation was less than 0.2%. The denudation analysis of each point was carried out for 80 s, including instrument background value acquisition for 20 s, laser denudation sample signal acquisition for 40 s, and purge time for 20 s. A set of standard samples was inserted and analyzed after every 10 sample points. Data processing was completed using GLITTER software. NIST610 was used as the standard sample, and Si was used as the internal standard element. The content of SiO_2 in the emerald sample was 66.9%. Compared with the standard value, the error of main elements was less than 5%, and the error of trace elements was less than 10%.

The UV/Vis/NIR spectrometer model was a GEM 3000 (BiaoQi Guangzhou, China) series, with the following test conditions: reflected light, integration time of 150 ms, average time of 30, smoothness of 2, and wavelength range of 220 to 1000 nm.

Ethiopian emeralds were tested using a mid-infrared spectrometer and a near-infrared spectrometer. The mid-infrared test range was 4000 to 400 cm^{-1}, the resolution was 4 cm^{-1}, and the number of collections was 64. The reflection method was carried out on a Nicolet iS5 IR spectrometer with a PIKE Up IR attachment, and the transmission method was carried out on a Nicolet iS5 IR spectrometer with a BEAM condenser attachment. The near-infrared band was tested using the reflection method with a type IR spectrometer Nicolet6700 featuring a calibrating SPHERE attachment; the test range was 4000 to 11,000 cm^{-1}, with a resolution of 4 cm^{-1}, and 64 collections.

The Raman spectrometer instrument model was a Renishaw inVia, with a power supply voltage of 220 V, current of 10 A, power frequency of 50 to 60 Hz, and test room temperature of 22 °C. A laser was used to identify the composition of inclusions, with a test range of 0 to 1500 cm^{-1} and 10 scans. The fluid inclusions were tested by depth scanning, and 200 points were collected at each position with a point distance of 2 μm. The 478 nm and 532 nm lasers were used to scan the fluid inclusions in sections. However, the 532 nm laser was used to scan the fluid inclusions in the test range of 0 to 1800 cm^{-1}, while the 478 nm laser was used to scan the fluid inclusions in the test range of 1800 to 3800 cm^{-1}.

4. Results and Discussion

4.1. Gemological Properties

The study sample numbers of Ethiopian emeralds were categorized as E-1 to E-7, and the conventional gemological properties of emeralds are shown in Table 1. A refractometer with a near-sodium equivalent light source was used to measure refractive indices (R.I.).

The results show that the refractive index of Ethiopian emeralds ranged from 1.578 to 1.593. The birefringence was 0.008 to 0.015.

Table 1. Conventional gemological properties of Ethiopian emeralds.

NUM.	Color	Weight/g	Shape	Refractive Index	Birefringence	Specific Gravity	Internal Features	Chelsea Filter	Fluorescence (LW/SW)
E-1	Green	0.218	Oval	1.578–1.592	0.014	2.735	Two- and three-phase fluid inclusions, typically tubular or rectangular. Mineral inclusions: the black sheet inclusions.	None	Inert/inert
E-2	Green	0.113	Oval	1.578–1.593	0.015	2.757	Two-phase inclusions, gas, or liquids. Mineral inclusions: flake inclusions (mica sheets).	None	Inert/inert
E-3	Deep green	0.274	Cushion	1.581–1.589	0.008	2.754	Two- and three-phase fluid inclusions, typically long tubular short tubular or rectangular. Partially healed fissures.	None	Inert/inert
E-4	Deep green	0.329	Truncated rectangle	1.580–1.592	0.012	2.732	Two- and three-phase fluid inclusions, typically short tubular or rectangular.	None	Inert/inert
E-5	Deep green	0.379	Oval	1.580–1.593	0.013	2.748	Two- and three-phase fluid inclusions, typically short tubular, rectangular or long tubular.	None	Inert/inert
E-6	Deep (light) green	17.538	Hexagonal column	No = 1.580–1.591 Ne = 1.569–1.584		2.722	The rich healed fissures reduce the transparency of the sample. Mineral inclusions: a large number of black flake inclusions. Hexagonal color zoning occurs vertical C-axis and can be seen that there are penetrate twin with longitudinal lines.	None	Inert/inert
E-7	Deep (light) green	23.916	Hexagonal column	No = 1.580–1.590 Ne = 1.569–1.584		2.699 (affected by surrounding rock)	The rich healed fissures reduce the transparency of the sample. A large number of colorless or white long tubular inclusions. Mineral inclusions: a large number of black flake inclusions.	None	Inert/inert

Through the Chelsea filter, all samples did not turn red, which may be related to the low content of Cr and V, as further tested below. Ethiopian emeralds are typically inert to long- and short-wave UV radiation. The apparatus for the hydrostatic specific gravity test shows that the specific gravity varied from 2.722 to 2.757, with an average specific gravity of 2.74.

4.2. Magnification

Ethiopian emeralds are rich in inclusions, including two-phase (CO_2 + H_2O, identified from Raman spectra), three-phase, and long tubular inclusions (Figure 3a,b), as well as black flake inclusions (biotite, identified from Raman spectra) (Figure 3c). On E-6 and E-7, a large number of black flake inclusions can be seen densely distributed in the crystal (Figure 3d), and some of them are exposed on the surface, affecting the overall transparency.

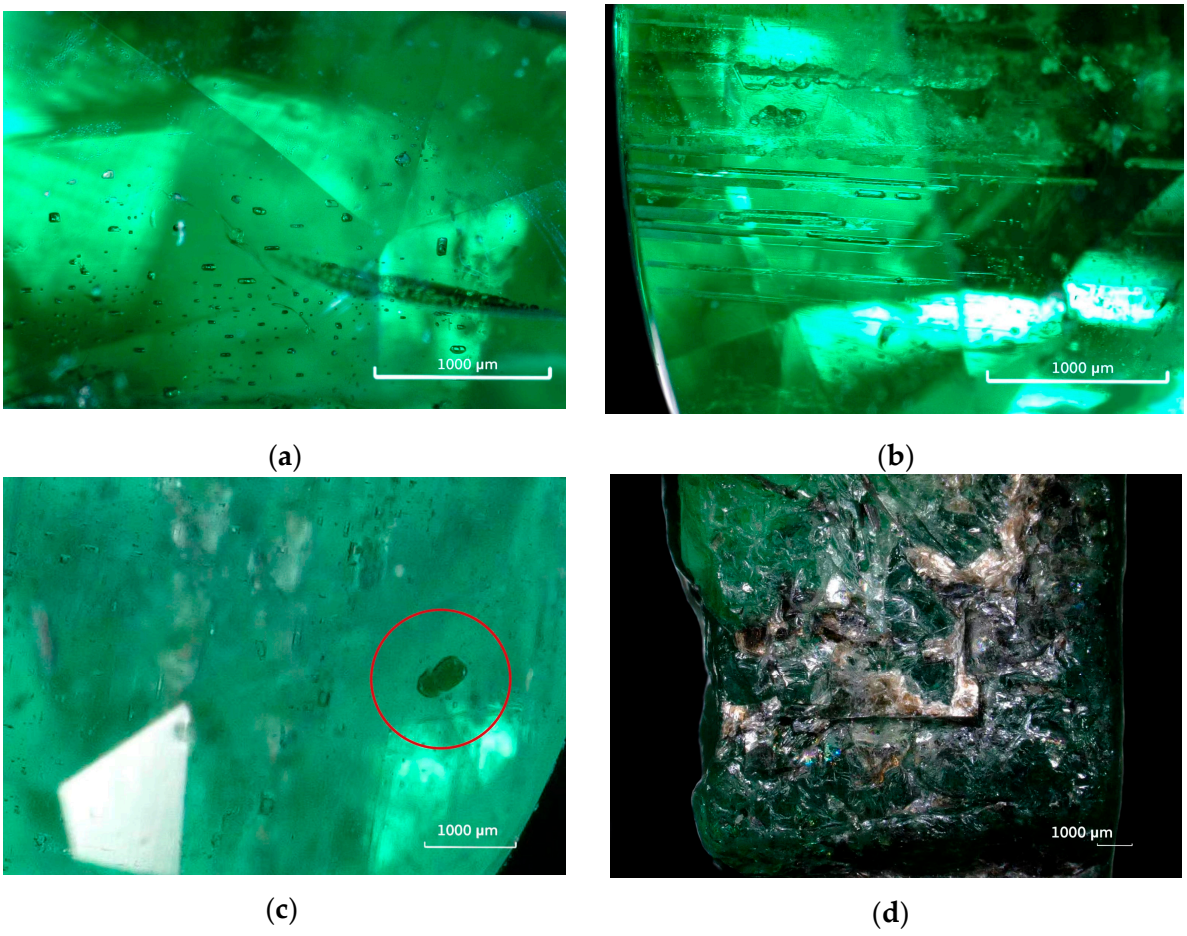


Figure 3. (**a**) Short columnar two-phase or three-phase inclusions in E-3; (**b**) long tubular inclusions in E-3; (**c**) dark mineral inclusions (the red circle) in E-1; (**d**) large amount of mica exposed on E-6.

4.3. Major and Trace Elements Analysis

4.3.1. EDXRF

The EDXRF test results are listed in Table 2. All samples were tested in different locations, and 20 groups of EDXRF results were obtained. The average values of the results of different test points in the same sample are plotted in Table 2. The results indicate the contents of all elements but are presented in the form of oxides. Since the experiment could not reach the vacuum condition, the test results start from element 13. FeO in the test result represents the total content of iron oxides, Fe_2O_3 and FeO, as the instrument could not distinguish the iron valence state. The Cr_2O_3, V_2O_3, and FeO contents in Ethiopian emeralds ranged from 0.35 to 1.81 wt.%, 0.06 to 0.18 wt.%, and 2.20 to 2.77 wt.%, respectively.

According to previous studies, emeralds are colored by chromium, vanadium, and iron [16–18]. Therefore, these three elements were selected for the ternary diagram to see the sample distribution. Twenty groups of EDXRF data from Ethiopia were combined with the sample data from other major regions of emeralds in the world. As shown in Figure 4, Ethiopian emeralds are mostly distributed in the upper part of the triangle, with a high content of FeO, followed by Cr_2O_3 and V_2O_3. Compared with emeralds from other locations, the area of triangular casting points is close to the oxides of emeralds in Zambia, which are low in Cr_2O_3, very low in V_2O_3, and high in FeO [19,33–35]. There are obvious differences in the content of FeO, Cr_2O_3, and V_2O_3 between the emeralds from Ethiopia and Colombia, which is the most important origin.

Table 2. EDXRF data of Ethiopian emerald (wt.%).

Samples		SiO_2	Al_2O_3	FeO	V_2O_3	Cr_2O_3	CaO	K_2O	ZnO	Rb_2O	SO_3
E-1	Range (two groups)	83.254–83.904	11.453–12.026	2.177–2.517	0.061–0.062	0.237–0.416	bdl	0.242–0.282	0.035–0.065	0.029–0.031	0.558–0.58
	Average	83.58	11.74	2.35	0.06	0.35	bdl	0.26	0.05	0.03	0.57
E-2	Range (two groups)	82.157–83.807	11.802–12.398	2.154–2.642	0.057–0.081	0.477–0.845	0.136–0.186	0.154–0.204	0.021–0.039	0.031–0.032	0.547–0.573
	Average	82.98	12.10	2.40	0.07	0.66	0.16	0.18	0.03	0.03	0.56
E-3	Range (two groups)	81.768–82.414	10.879–11.781	2.232–2.586	0.132–0.228	1.358–1.666	0.128–0.174	bdl	0.023–0.037	0.035–0.045	0.632–0.76
	Average	82.09	11.33	2.41	0.18	1.51	0.15	bdl	0.03	0.04	0.65
E-4	Range (two groups)	81.232–82.988	11.454–13.952	2.034–2.372	0.087–0.137	1.272–1.49	0.108–0.13	bdl	0.017–0.043	0.030–0.031	0.743–0.871
	Average	82.11	12.70	2.20	0.11	1.38	0.12	bdl	0.03	0.03	0.81
E-5	Range (two groups)	82.776–83.544	10.324–10.914	2.534–2.788	0.066–0.1	1.567–2.053	0.103–0.119	0.225–0.277	0.021–0.039	0.027–0.033	0.543–0.861
	Average	83.16	10.62	2.66	0.08	1.81	0.11	0.25	0.03	0.03	0.7
E-6	Range (five groups)	80.789–83.258	10.949–12.653	2.137–2.931	bdl-0.137	0.165–1.152	0.127–0.852	0.549–1.675	0.027–0.046	0.023–0.048	bdl-2.949
	Average	81.38	11.60	2.77	0.06	0.64	0.47	1.40	0.03	0.03	0.97
E-7	Range (five groups)	76.671–84.687	10.770–12.169	1.999–4.233	bdl–0.153	0.587–1.324	0.174–0.994	bdl–3.462	0.019–0.044	0.024–0.051	bdl–1.452
	Average	82.40	11.53	2.58	0.07	0.74	0.32	0.87	0.03	0.03	1.09

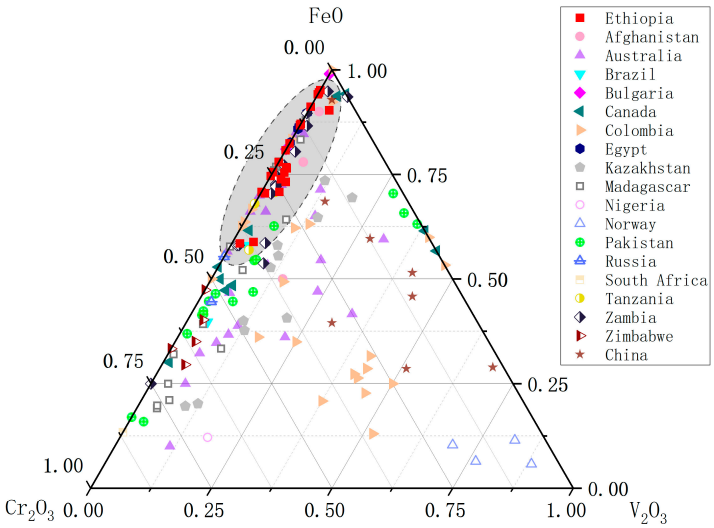


Figure 4. Ternary plot of relative abundance of Cr_2O_3, V_2O_3, and FeO in emerald samples from Ethiopia (red squares). Other sources are from [3,33–37].

4.3.2. LA-ICP-MS

The LA-ICP-MS test results (Table 3) show that Ethiopian emeralds tended to have high concentrations of alkali metal ions (Li, Na, K, Rb, and Cs), ranging from 14,022 to 14,633 ppmw (average 14,333 ppmw). The contents of alkali metals were relatively stable in all samples tested. Li contents ranged from 258.74 to 351.14 ppmw (average 313.80 ppmw). Cs contents ranged from 324.45 to 423.98 ppmw (average 382.43 ppmw). Chromophore concentrations of Cr, V, and Fe were 734.34 to 1644.3 ppmw (average 1269.13 ppmw), 89.61 to 106.61 ppmw (average 97.44 ppmw), and 4468.04 to 5022.3 ppmw (average 4678.34 ppmw), respectively. The concentrations of Cr were greater than those of V, and the Cr/V ratio ranged from 8.12 to 16.43. The emerald crystals also contained certain amounts of Sc (33.02 to 55.33 ppmw), Zn (52.7 to 67.84 ppmw), Na (12,599 to 13,562 ppmw), Rb (64.18 to 70.04 ppmw), and other elements (Table 3).

Table 3. Chemical composition (average) of Ethiopian emeralds by LA-ICP-MS (in ppmw).

Sample		E-1	E-2	E-3	E-4	E-5	E-6	E-7	Detection Limit
Element									
Li	Range Average	258.74	295.16	337.95	334	351.14	269.34–339.12 298.67	279.94–328.5 307.65	0.916
Be	Range Average	57,678.31	58,712.61	58,364.298	56,583.117	58,187.88	55,626.5–58,257.27 57172.33	54,531.711–58,836.23 56,703.13	5.08
B	Range Average	2.06	2.49	2.98	2.36	2.33	2.26–4.22 3.36	2.51–2.66 2.59	2.05
Na	Range Average	13,187.93	13,077.7	13,375.43	13,358.53	13,562.31	12,893.51–13,427.85 13122.65	12,599.09–13,271.39 12,951.83	11.19
Al	Range Average	83,606.16	82,635.77	97,151.76	94,116.54	96,336.16	83,120.97–95,013.34 89361.67	89,020.84–91,747.15 90,464.23	2.59
P	Range Average	40.52	50.76	54.79	57	58.77	45.64–55.79 50.43	54.93–56.56 55.78	5.61
K	Range Average	338.37	342.88	337.18	336.54	325.39	323.05–351.78 340.26	307.73–361.21 337.28	4.12
Ca	Range Average	324.3	338.15	443	517.11	448.61	314.84–472.98 395.27	305.38–469.61 390.21	25.4
Sc	Range Average	33.02	33.37	55.33	53.03	53.76	33.195–53.54 44.99	36.34–50.88 42.89	0.124
Ti	Range Average	85.34	85.01	118.51	121.45	149.38	83.38–117.08 101.79	81.42–114.47 102.29	0.594
V	Range Average	92.56	92.9	97.86	106.61	99.2	91.085–102.3 97.023	89.61–100.59 95.20	0.0759
Cr	Range Average	751.98	858.25	1537	1644.34	1629.96	743.16–1639.78 1323.59	734.34–1621.82 1260.25	1.98
Mn	Range Average	30.97	25.41	42.76	37.53	29.84	24.79–44.67 35.15	18.61–44.14 33.12	0.293
Fe	Range Average	4483.25	4544.32	4736.51	5022.31	4699.8	4475.675–5000.95 4814.33	4468.04–4661.89 4552.68	9.32
Co	Range Average	1.71	1.444	1.346	1.499	1.515	1.408–1.577 1.493	1.38–1.442 1.408	0.0772
Ni	Range Average	15.96	13.9	9.89	10.54	8.3	9.1–14.93 11.86	10.75–13.37 12.22	1.73
Zn	Range Average	58.62	60.65	58.08	67.84	57.69	55.66–63.58 60.16	52.7–58.43 55.79	0.404
Ga	Range Average	21.97	22.06	21.44	24.24	21.94	21.04–22.56 21.86	21.63–21.85 21.75	0.0948
Rb	Range Average	68.32	68.54	66.09	69.97	70.04	65.855–69.91 68.25	64.18–68.42 66.2	0.154
Sn	Range Average	0.97	0.84	0.72	0.9	bdl	0.6–0.905 0.79	0.62–0.96 0.806	0.4
Cs	Range Average	407.07	422.67	346.85	346.86	324.45	332.81–415.525 401.62	340.88–423.98 387.83	0.0621
Th	Range Average	bdl	0.0011	0.001	0.001	bdl	bdl	bdl	0.001
U	Range Average	bdl	0.00093	bdl	bdl	bdl	bdl–0.00069 bdl	bdl	0.0001

bdl = below detection limit; values for E-6 and E-7 are data ranges.

There are limited data on trace elements published for Ethiopian emeralds, and only a few groups of data are generally used for origin comparison [9]. In this study, seven Ethiopian emeralds were analyzed using LA-ICP-MS. When determining gemological origin, plots of trace elements are used to detect possible correlations. Therefore, it was necessary to add LA-ICP-MS data from other major emerald deposits around the world, such as Afghanistan, Madagascar, Zambia, Brazil, and Colombia [37–42]. To further explore the discrimination, a series of binary diagrams and a triangular diagram were constructed.

In the binary diagram of Li and Cs (Figure 5), the results of tested Ethiopian emeralds showed significant differences from other sources. The contents of Cs and Li in Zambia were relatively higher than those of Ethiopian emeralds tested in this study. The content of Cs in Madagascar emeralds was partly higher than that of Ethiopian emeralds, while Li

was usually lower. The content of Cs in Zimbabwe and Russia emeralds was partly higher than that of Ethiopian emeralds, while Li was usually higher. The contents of Cs and Li in other locations were relatively lower than those in Ethiopian emeralds.

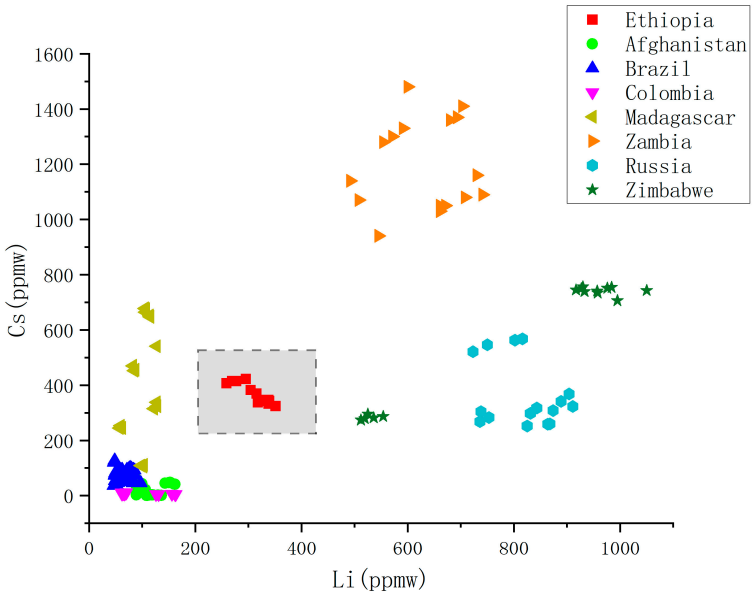


Figure 5. Plot of lithium (Li) versus cesium (Cs) concentrations from LA-ICP-MS analyses. Data are expressed in ppmw. Other sources are from [20,38–43].

In the binary diagram of Li and K (Figure 6), the results of tested Ethiopian emeralds fluctuated within an independent regional area, compared with other sources. The content of K in emeralds from Madagascar was significantly higher than those from Ethiopia. The contents of K in emeralds from Colombia and Russia were significantly lower than in those from Ethiopia. The contents of K and Li in Ethiopian emerald samples tested in this study were relatively intermediate, enabling them to be quickly compared with the emeralds in Zambia with high Li, in Madagascar with high K and low Li, and from other sources with low contents.

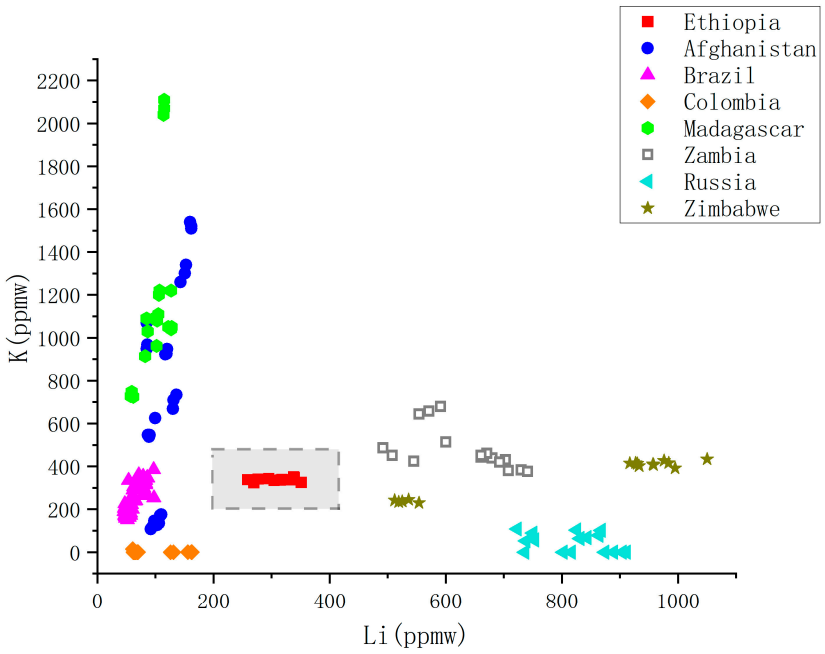


Figure 6. Plot of lithium (Li) versus potassium (K) concentrations from LA-ICP-MS analyses. Data are expressed in ppmw. Other sources are from [20,38–43].

When the emeralds from Ethiopia were distinguished from emeralds from Zambia and Brazil, the triangular diagram of the three trace elements, rubidium, cesium, and scandium, also showed obvious differences among the three sources (Figure 7). Emeralds from Ethiopia in the triangular diagram were located in an area of high Cs, low Rb, and low Sc. The Cs content in emeralds from Ethiopia was relatively higher than that in those from Brazil and lower than that of Zambia, while the Sc content in Zambian emeralds was relatively lower. In addition, the contents of Rb in Ethiopian emeralds were the same as those from Brazil and higher than in those from Zambia.

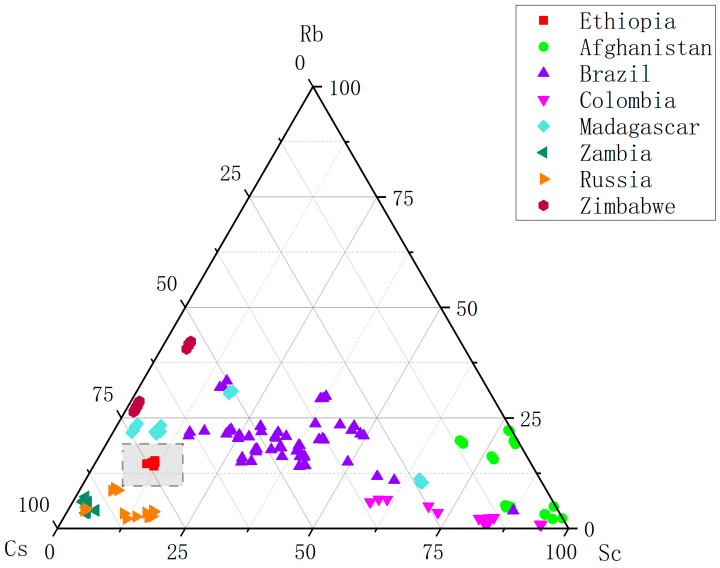


Figure 7. Ternary plot of relative abundance of rubidium (Rb), cesium (Cs), and scandium (Sc) in emerald samples from Ethiopia (red squares). Other sources are from [20,38–43].

The trace element concentrations of emeralds from the eight localities were plotted in a Zn-Li-Ga ternary diagram (Figure 8), which was quite effective at separating the emeralds from Russia, Madagascar, and Brazil (which are relatively close in Figure 7). Russian, Zambian, some Zimbabwean, and Madagascar emeralds were Li dominant, while some Colombian stones had intermediate Li-Ga contents. Emeralds from Brazil were Li-Zn dominant, whereas the Ethiopian specimens fall closer to the Ga side of the plot.

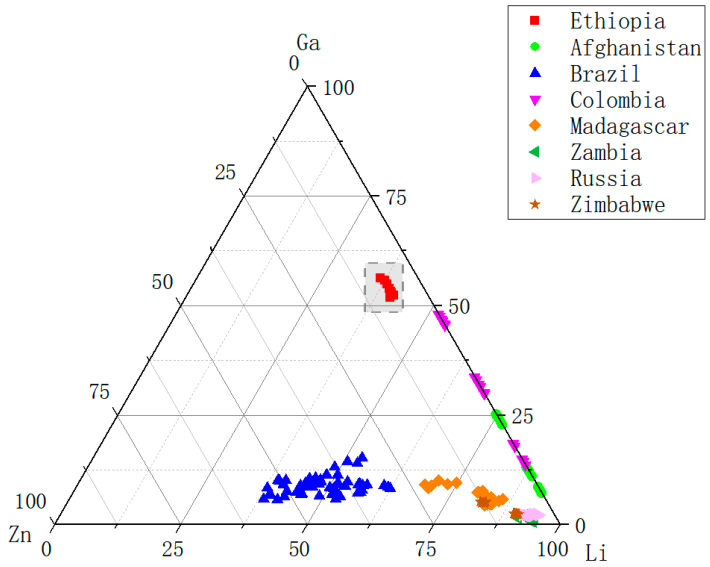


Figure 8. Ternary plot of relative abundance of gallium (Ga), zinc (Zn), and lithium (Li) in emerald samples from Ethiopia (red squares). Other sources are from [9,20,37–40].

The values of Cr/V in Ethiopian emeralds were investigated (Figure 9). The data results show that the content of Cr in emeralds from Ethiopia was partly lower than that in those from Brazil, which was similar to that in emeralds from Zambia and Russia, while it was significantly different from that in emeralds from other sources.

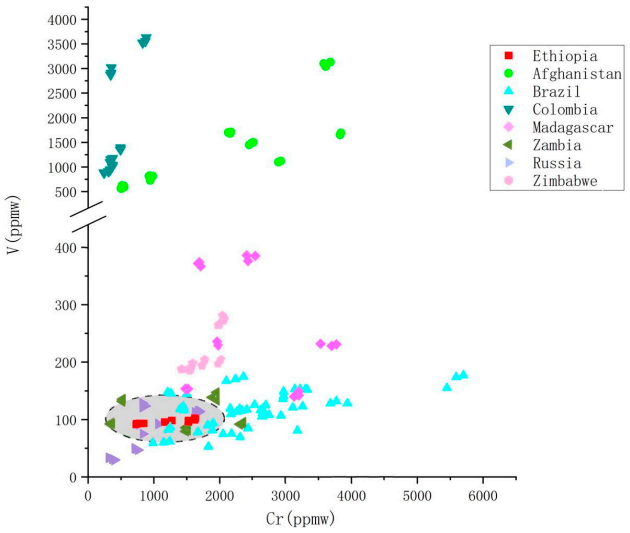
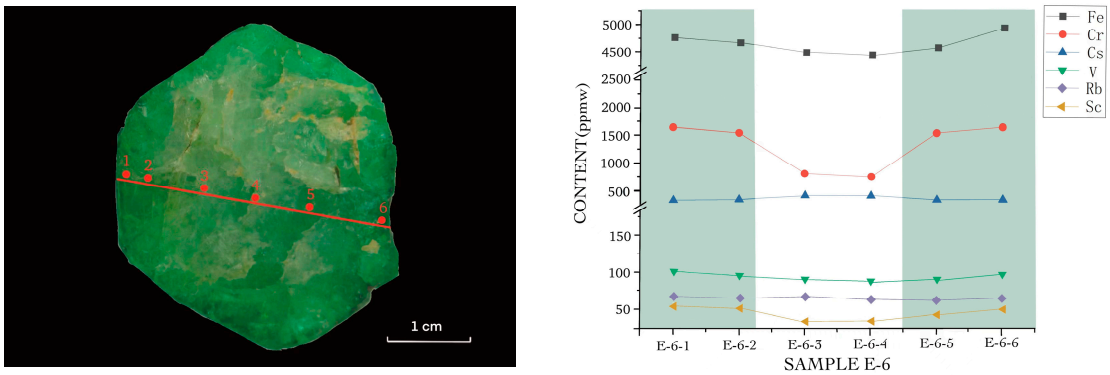


Figure 9. Plot of chromium (Cr) versus vanadium (V) concentrations from LA-ICP-MS analyses. Data are expressed in ppmw. Other sources are from [20,38–43].

The hexagonal color zoning, with light-green centers and green rims, can be observed clearly in the cross-section of the crystal C-axis, which oscillates between green and light-green zones with systematic variation in the zoning. It has about 60% light green centers with 40% green rims, and the borders of the hexagonal color zoning are blurred. In view of the color zone in the crystal, six points of the color gradient in E-6 were selected for LA-ICP-MS. The trace elements of each test point are plotted in Figure 10. The content of most elements was relatively stable in the crystal core, and it changed extensively from a light-green core to a medium-green edge, indicating that the growth environment of emeralds was relatively stable in the initial stage of crystallization [44]. The content of the Cr element increased significantly from the core to the edge, and the content of the V element increased slightly from the core to the edge, indicating that Cr played an important role in the green color of Ethiopian emerald, consistent with the EDXRF results.



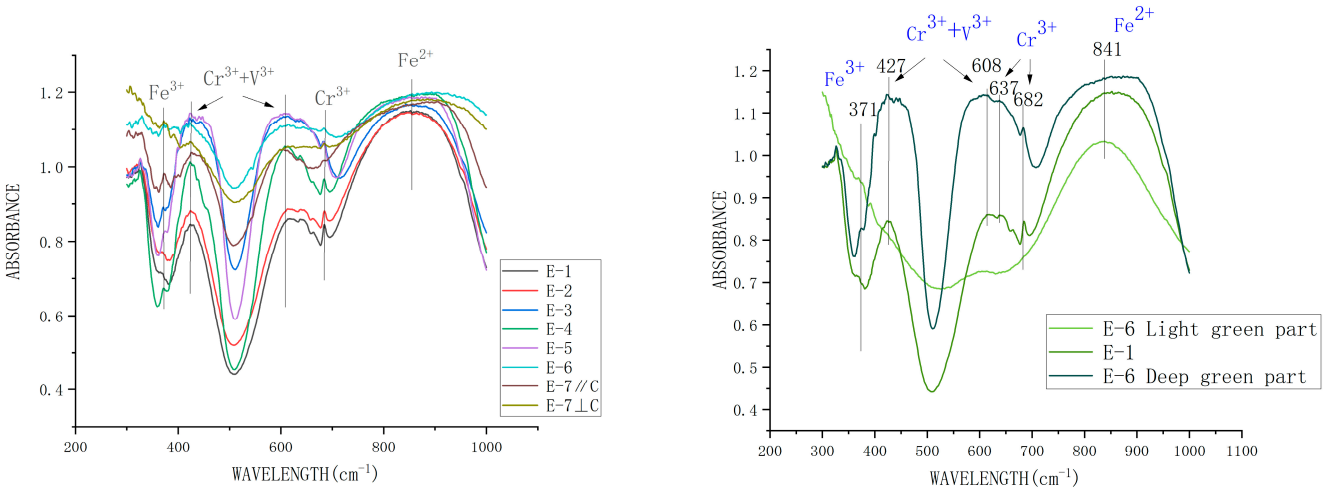
(**a**) (**b**)

Figure 10. (**a**) Representative photograph of color-zoned emerald crystal E-6 with a light-green core and a medium-green rim. The red points (1–6) indicate the positions of analysis. (**b**) LA-ICP-MS data for selected trace element analysis from E-6-1 to E-6-6. Plots of Fe, Cr, Cs, V, Rb, and Sc are used to highlight compositional changes.

4.4. Spectroscopy

4.4.1. UV/Vis/NIR

Cr and/or V elements are the main chromogenic elements of emeralds [16]. By selecting the typical spectra of samples with different color shades and analyzing the UV/Vis spectrum (Figure 11a), the mechanism underlying the color of emeralds in Ethiopia can be qualitatively studied.



(**a**) (**b**)

Figure 11. (**a**) UV/Vis spectra of Ethiopian emeralds (all samples). (**b**) UV/Vis spectra of Ethiopian emeralds (light green, green, and deep green from bottom to top).

The deep and light parts of the E-6 crystal were selected, and the test results are shown in Figure 11b according to the sequence of light green (the core of E-6), green (E-1), and deep green (the edge of E-6) from bottom to top.

The peak position and attribution of the ultraviolet spectrum of each sample within 300 to 900 nm are shown in Table 4.

Table 4. UV/Vis absorption spectra of Ethiopian emeralds.

Samples	Color	Characteristic Absorption Peak (nm)			
		Fe^{3+}	Cr^{3+}	Cr^{3+} + V^{3+}	Fe^{2+}
E-1	Green	–	638, 662, 684	423, 614	850
E-2	Green	–	637, 684	431, 608	848
E-3	Deep green	371	632, 683	427, 613	844
E-4	Deep green	369	637, 684	428, 608	846
E-5	Deep green	371	638, 682	422, 607	845
E-6	Light green	–	642, 665, 684	423, 614	864
	Deep green	371	642, 684	429, 608	846
E-7	Light green	–	637, 684	425, 604	861
	Deep green	371	637, 684	425, 604	861

As shown in Table 4, the main peaks of the UV/Vis absorption spectra of Ethiopian emerald samples were located at 371 nm, 425 nm, 608 nm, 637 nm, 662 nm, 684 nm, and 848 nm, and the peaks appeared similarly in all spectra.

The absorption peaks of both Cr^{3+} and V^{3+} appeared near the purple region (around 420 nm) and the orange-red region (about 620 nm) [16]. The absorption intensity of Cr^{3+} was slightly higher in the orange-red region, while that of V^{3+} was slightly higher in the purple region. As shown in the spectra (Figure 11), the intensity of absorption bands near the orange-red region and purple region of the spectra was similar. The absorption peaks

at 425 nm and 608 nm were produced by the joint action of Cr^{3+} and V^{3+} [16,45–48]. The characteristic absorption peaks of Cr^{3+} were at 637 nm, 662 nm, and 684 nm, and the emeralds colored by V^{3+} only did not show these three absorption peaks [47]. Therefore, Cr^{3+} was the major chromic ion of Ethiopian emeralds, consistent with the LA-ICP-MS results.

The absorption bands between 700 and 900 nm are caused by Fe^{2+} occupying different lattice positions [16,46]. The absorption band near 371 nm is related to Fe^{3+}, and its intensity is obviously lower [46]. As shown in Figure 11b, the absorption peak of Fe^{3+} was weak or even absent in light-green and green emeralds (E-6 light-green core and E-1 in Figure 11b), while it was relatively stronger in deep-green emeralds (E-6 deep-green edge in Figure 11b). This indicates that iron influenced the color of the emeralds. A darker color indicated a more obvious absorption of Fe^{3+}.

4.4.2. FTIR Spectroscopy

All samples were tested, and the results are shown in Figures 12 and 13.

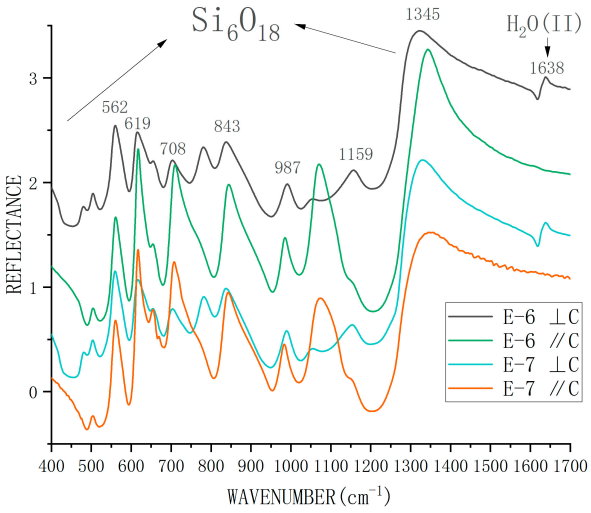
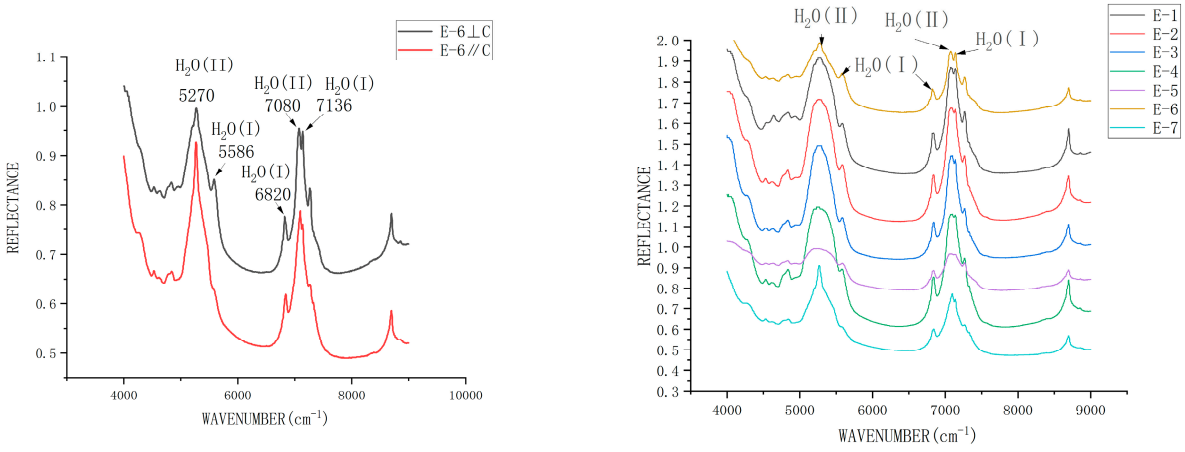


Figure 12. The representative FTIR spectrum in the range of 400–1700 cm^{-1} (E⊥C, E//C). The upper spectrum is vertically offset for clarity.



(**a**) (**b**)

Figure 13. (**a**) The representative FTIR spectrum in the range of 10,000–4000 cm^{-1} (E-6⊥C, E-6//C) illustrating type I and type II H_2O observed in Ethiopian emeralds. (**b**) The representative FTIR spectrum in the range of 10,000–4000 cm^{-1} (all samples) illustrating type I and type II H_2O observed in Ethiopian emeralds. The upper spectrum is vertically offset for clarity.

Beryl is a ring silicate mineral, and its fingerprint region absorption (400–1500 cm^{-1}) in the infrared spectrum is mainly caused by the vibration of [Si_6O_{18}] and other groups [16]. As shown in Figure 11, the absorption peaks of $\nu_{Si-O-Si}$, and ν_{O-Si-O} appeared in the range from 1053 to 1159 cm^{-1} and from 985 to 993 cm^{-1} [16,49]. The absorption peak of medium strength from 615 to 845 cm^{-1} was caused by the symmetric stretching vibration of $\nu_{Si-O-Si}$. However, the bands below 600 cm^{-1} were caused by the bending vibration δ_{Si-O} and stretching vibration ν_{M-O}, as well as their coupling vibration [49,50].

It can be seen from the infrared spectrum of Ethiopian emeralds that there was an absorption peak of 1638 cm^{-1} caused by H_2O bending vibration in the mid-infrared region in the direction perpendicular to the C-axis, while there was no absorption in the direction parallel to the C-axis [14].

Strong absorption peaks near 7080 cm^{-1}, 7136 cm^{-1}, and 5270 cm^{-1} can be seen in the NIR spectra in Figure 13, which were caused by the vibration of type II H_2O (symmetry axis is perpendicular to the c-axis) [16], while the vibrations of type I H_2O (symmetry axis is parallel to the c-axis) were at 5586 cm^{-1} and 6820 cm^{-1}, which were relatively weaker [16,49]. The absorption peak at 7080 cm^{-1} was positively correlated with the absorption peak caused by Na–H, and the increase in Na^+ in the channel led to an increase in type II H_2O content [51]. This indicates that there was more type II H_2O than type I H_2O in Ethiopian emeralds, which is related to the high content of alkali metals in emeralds, as also proven by the LA-ICP-MS results.

4.5. Raman Spectroscopy

The Ethiopian emeralds and their inner inclusions were subjected to laser Raman analysis, and representative data are shown in Figure 14.

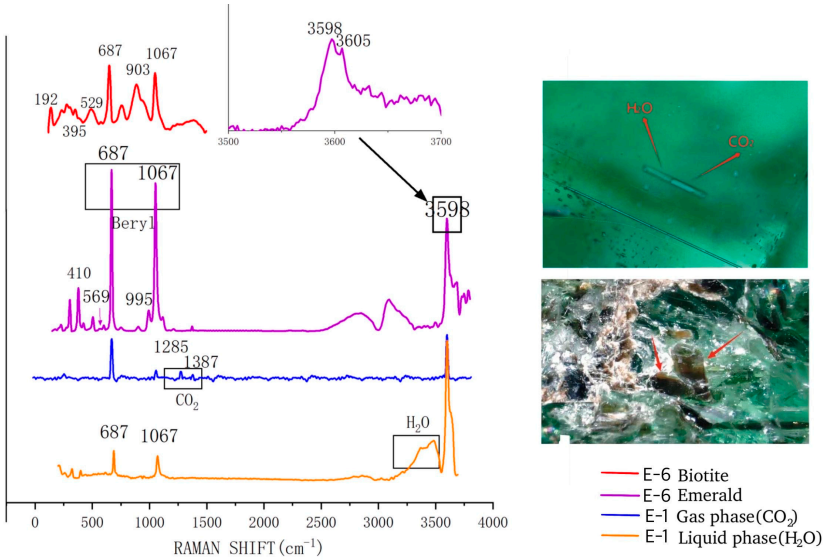


Figure 14. Raman spectra from 0 to 3800 cm^{-1} of an emerald from Ethiopia (from top to bottom: the biotite peak, emerald peak, gas phase peak, and liquid phase peak). The upper spectrum is vertically offset for clarity.

It can be seen that the main Raman peaks of the Ethiopian emerald Raman spectrum were 410 cm^{-1}, 569 cm^{-1}, 687 cm^{-1}, 995 cm^{-1}, and 1067 cm^{-1}. The peaks located at 687 cm^{-1} and 1067 cm^{-1} indicate the characteristic vibration frequencies of the [Si_6O_{18}], [BeO_4], and [AlO_6] groups in the emerald crystal structure [52].

The peak around 687 cm^{-1} was due to Be–O stretching vibrations, and the peak around 1067 cm^{-1} was due to Si–O and/or Be–O stretching [48–50]. These two peaks could be attributed to beryl, representing the characteristic peaks of emeralds [52]. In the [A1O_6] octahedron, the bending vibration peak of Al–O is at 410 cm^{-1} [52–54]. The peaks ranging from 800 cm^{-1} to 1200 cm^{-1} corresponded to the symmetric and antisymmetric stretching

vibrations of the Si–O bond. The peak at 995 cm^{-1} was caused by the symmetric stretching vibration of Be–O (BeO_4), and the peak at 569 cm^{-1} was the Raman scattering peak formed by the bending vibration of O–Be–O in the tetrahedron [48–50,52–56].

There was an obvious split double peak at about 3600 cm^{-1}, which was related to the stretching vibration peak of water molecules. The stretching vibration of type II H_2O molecules was at 3598 cm^{-1}, and the stretching vibration of type I H_2O molecules was at 3605 cm^{-1} [50,52,53]. The I_{3605} was lower than I_{3598}, which is consistent with the FTIR results.

The laser focused on the fluid inclusions. The Raman spectra reveal characteristic vibration peaks at 1285 cm^{-1} and 1387 cm^{-1}, which coincide with the characteristic peaks of CO_2 [48,49]. There is an obvious broad "hump-like" peak between 3200 cm^{-1} and 3500 cm^{-1}, which can be proven to be the characteristic peak of liquid H_2O [52]. It can be concluded that, in the two-phase inclusions of emeralds in Ethiopia, the gaseous component was CO_2 and the liquid component was H_2O. The emerald dark flake inclusions in the Raman test results were indicated by the characteristic absorption peaks at 192 cm^{-1}, 395 cm^{-1}, 529 cm^{-1}, and 903 cm^{-1}, which were identical to those of biotite [32]. Therefore, the dark flake inclusions in the emeralds of Ethiopia were biotite sheets, consistent with the tectonic-magmatic-related geological environment of the region.

5. Conclusions

The EDXRF and UV/Vis tests showed that Cr was the major chromogenic element of Ethiopian emeralds, and the Cr content changed notably across color zones. The content of Fe was high, influencing the color of the emeralds, while the content of V was low.

The LA-ICP-MS results showed a high content of alkali metals (Li, Na, K, Rb, and Cs), ranging from 14,022 to 14,633 ppmw, indicating the tectonic-magmatic-related geological environment of the deposit. According to this study, emeralds from Ethiopia can be distinguished from other sources by the content of alkali metals (Li, Na, K, Rb, and Cs) and some trace elements (Sc, V, Cr, and Fe).

The FTIR and Raman spectra displayed more type II H_2O than type I H_2O in the emeralds from Ethiopia. There were two main inclusions, gas–liquid two-phase inclusions constituting CO_2 and H_2O, and dark crystal, mainly constituting biotite sheets, in Ethiopian emeralds. Both type II H_2O and biotite inclusions were related to the high content of alkali metals, consistent with the LA-ICP-MS results.

Author Contributions: Conceptualization, Z.H. and G.L.; methodology, Z.H.; software, Z.H. and L.W.; validation, Z.H., L.W., M.Z. and G.L.; formal analysis, Z.H. and L.W.; investigation, G.L.; resources, M.Z. and L.W.; data curation, Z.H.; writing—original draft preparation, Z.H.; writing—review and editing, Z.H., L.W., M.Z. and G.L.; visualization, Z.H. and G.L.; supervision, M.Z. and G.L.; project administration, G.L.; funding acquisition, G.L. All authors have read and agreed to the published version of the manuscript.

Funding: This research received no external funding.

Data Availability Statement: Not applicable.

Conflicts of Interest: The authors declare no conflict of interest.

References

1. Fritsch, E.; Rossman, G. An update on color in gems Part 3: Colors caused by band gaps and physical phenomena. *Gems Gemol.* **1988**, *24*, 81–103. [CrossRef]
2. Nicol, C.A.; Marshall, D.; Einfalt, H.C.; Thorkelosn, D. Pressure-Temperature-Fluid Constraints for the Formation of the Halo-Shakiso Emerald Deposit, Southern Ethiopia: Fluid Inclusion and Stable Isotope Studies. *Can. Mineral.* **2022**, *60*, 29–48.
3. Groat, L.A.; Giuliani, G.; Marshall, D.D.; Turner, D. Emerald deposits and occurrences: A review. *Ore Geol. Rev.* **2008**, *34*, 87–112. [CrossRef]
4. Rondeau, B. Matériaux Gemmes de Référence du Museum National D'Histoire Naturelle: Exemples de Valorisation Scientififique d'une Collection de Minéralogie et Gemmologie. Ph.D. Thesis, University of Nantes, Nantes, France, 2003.

5. Strack, E.; Kostov, R.I. Emeralds, sapphires, pearls and other gemmological materials from the Preslav gold treasure (X century) in Bulgaria. *Geochem. Minerals* **2010**, *48*, 103–123.
6. Karampelas, S.; Wörle, W.; Hunger, K.; Hanspeter, L. Micro-Raman spectroscopy on two chalices from the Benedictine Abbey of Einsiedeln: Identification of gemstones. *J. Raman Spectrosc.* **2012**, *43*, 1833–1838. [CrossRef]
7. Farges, F.; Panczer, G.; Benbalagh, N.; Riondet, G. The Grand Sapphire of Louis XIV and The Ruspoli Sapphire. *Gems Gemol.* **2015**, *51*, 392–409. [CrossRef]
8. Panczer, G.; Riondet, G.; Forest, L.; Krzemnicki, M.S.; Carole, D.; Faure, F. The Talisman of Charlemagne: New Historical and Gemological Discoveries. *Gems Gemol.* **2019**, *55*, 40–46. [CrossRef]
9. Aurisicchio, C.; Conte, A.M.; Medeghini, L.; Ottolini, L.; De Vito, C. Major and trace element geochemistry of emerald from several deposits: Implications for genetic models and classification schemes. *Ore Geol. Rev.* **2018**, *94*, 351–366. [CrossRef]
10. Gonthier, E. The symbolic representation of famous emeralds. In *L'Émeraude*; Giard, D., Giuliani, G., Cheilletz, A., Fritch, E., Gonthier, E., Eds.; AFG-CNRS-ORSTOM Edition: Paris, France, 1998; pp. 27–32.
11. Hänni, H.A. Origin determination for gemstones: Possibilities, restrictions and reliability. *J. Gemmol.* **1994**, *24*, 139–148. [CrossRef]
12. Schwarz, D.; Giuliani, G.; Grundmann, G.; Glas, M. The origin of emerald—A controversial topic. *Extralapis Engl.* **2002**, *2*, 18–21.
13. Krzemnicki, M.S. Determining the origin of gemstones: Challenges and perspectives. *InColor* **2007**, *4*, 6–11.
14. Groat, L.; Giuliani, G.; Marshall, D.; Turner, D. Emerald. In *Geology of Gem Deposits*; Raeside, E.R., Ed.; Mineralogical Association of Canada: Tucson, AZ, USA, 2014; Volume 44, pp. 135–174.
15. Giuliani, G.; Chaussidon, M.; Schubnel, H.J.; Piat, D.; Rollion-Bard, C.; France-Lanord, C.; Giard, D.; de Narvaez, D.; Rondeau, B. Oxygen isotopes and emerald trade routes since antiquity. *Science* **2000**, *287*, 631–633. [CrossRef] [PubMed]
16. Wood, D.L.; Nassau, K. The characterization of beryl and emerald by visible and infrared absorption spectroscopy. *Am. Mineral.* **1968**, *53*, 777–799.
17. Huong, L.T.T. Microscopic, Chemical and Spectroscopic Investigations on Emeralds of Various Origins. Ph.D. Thesis, University of Mainz, Mainz, Germany, 2008.
18. Moroz, I.; Roth, M.L.; Deich, V.B. The visible absorption spectroscopy of emeralds from different deposits. *Aust. Gemmol.* **1999**, *20*, 315–320.
19. Fritsch, E. Gem News International. *Gems Gemol.* **2012**, *48*, 306–311. [CrossRef]
20. Cevallos, P.; Simmons, W.B.; Falster, A.U. Gem News International: Emerald from Ethiopia. *Gems Gemol.* **2012**, *48*, 219–221.
21. Laurs, B.M. New production of emerald from Ethiopia. *J. Gemmol.* **2017**, *35*, 386–387.
22. Roland, S.; Naryratha, H.S. Emeralds from Ethiopia. *GemGuide* **2018**, *37*, 4–8.
23. Ahmadjan, A. *The Science of Gemstones*; Ark Publishing: Tokyo, Japan, 2019; pp. 106–110.
24. Karampelas, S.; Al-Shaybani, B.; Mohamed, F.; Sangsawong, S.; Al-Alawi, A. Emeralds from the Most Important Occurrences: Chemical and Spectroscopic Data. *Minerals* **2019**, *9*, 561. [CrossRef]
25. Abbate, E.; Bruni, P.; Sagri, M. Geology of Ethiopia: A review and geomorphological perspectives. In *Landscapes and Landforms of Ethiopia*; Springer: Berlin/Heidelberg, Germany, 2015; pp. 33–64.
26. Yibas, B.; Reimold, W.; Armstrong, R.; Koeberl, C.; Anhaeusser, C.R.; Phillips, D. The tectonostratigraphy, granitoid/geochronology and geological evolution of the Precambrian of southern Ethiopia. *J. Afr. Earth Sci.* **2002**, *34*, 57–84. [CrossRef]
27. Solomon, T. Geochemistry of the pegmatitic rocks and minerals in the Kenticha Belt, Southern Ethiopia: Implication to geological setting. *Gondwana Res.* **2001**, *4*, 97–104.
28. Vactora, M. Geological and geochemical study of gold and base metal mineralization in the Surupa region of Borena region in southern Ethiopia. *Petrochem. Indian Int.* **2022**, *5*, 107–117.
29. Gao, C.; Dang, W.; Tian, S.; Qi, X.; Peng, W.; Chen, Y. Geological features and mineral profiles of Ethiopia. *Shandong Land Resour.* **2011**, *11*, 19–23. (In Chinese)
30. Merera, W. Preliminary Geological and Geochemical Study of Gold and Base Metals Mineralization in The Surupa Area, Borena Zone, Southern Ethiopia. *Res. Sq.* **2021**. [CrossRef]
31. Desta, Z.; Garbarino, C.; Valera, R. Granite Pegmatite System in Kenticha (Adola, Sidamo, Ethiopia) Rare Metal Pegmatite Belt: Petrochemistry, Regional Pegmatite Zoning and Classification. *Ethiop. J. Sci.* **1995**, *18*, 119–148.
32. Mohammed, S.M.; Zerihun, D.; Getaneh, D. Petrography and geochemistry of the primary ore zone of the Kenticha rare metal granite-pegmatite field, Adola Belt, Southern Ethiopia: Implications for ore genesis and tectonic setting. *J. Afr. Earth Sci.* **2017**, *134*, 73–84. [CrossRef]
33. Schwarz, D. Australian emeralds. *Aust. Gemmol.* **1991**, *17*, 488–497.
34. Kozlowski, A.; Metz, P.; Estrada Jaramillo, H.A. Emeralds from Somondoco, Colombia: Chemical composition, fluid inclusions and origin. *Neues Jahrb. Mineral.* **1988**, *159*, 23–49.
35. Zwaan, J.C.; Seifert, A.; Vrána, S.; Laurs, B.M.; Anckar, B.; Simmons, W.B.; Falster, A.U.; Lustenhouwer, W.J.; Muhlmeister, S.; Koivula, J.I.; et al. Emeralds from the Kafubu area, Zambia. *Gems Gemol.* **2005**, *41*, 116–148. [CrossRef]
36. Vapnik, Y.; Moroz, I.; Eliezri, I. Formation of emeralds at pegmatite-ultramafic contacts based on fluid inclusions in Kianjavato emerald, Mananjary deposits, Madagascar. *Mineral. Mag.* **2006**, *70*, 141–158. [CrossRef]
37. Cartier, L.E.; Ali, S.H.; Krzemnicki, M.S. Blockchain, chain of custody and trace elements: An overview of tracking and traceability opportunities in the gem. *J. Gemmol.* **2018**, *36*, 212–227. [CrossRef]

38. Hänni, H.A.; Schwarz, D.; Fischer, M. The emeralds of the Belmont mine, Minas Gerais, Brazil. *J. Gemmol.* **1987**, *53*, 446–456. [CrossRef]
39. Schmetzer, K.; Bernhardt, H.; Biehler, R. Emeralds from the Ural Mountains, USSR. *Gems Gemol.* **1991**, *27*, 86–99. [CrossRef]
40. Schwarz, D. Emeralds from the Mananjary region, Madagascar: Internal features. *Gems Gemol.* **1994**, *30*, 88–101. [CrossRef]
41. Zwaan, J.C.; Kanis, J.; Petsch, J. Update on emeralds from the Sandawana mines, Zimbabwe. *Gems Gemol.* **1997**, *33*, 80–101. [CrossRef]
42. Kievlenko, E.Y. Beryl. In *Geology of Gems*, 1st ed.; Soregaroli, A., Ed.; Ocean Pictures Ltd.: Littleton, CO, USA, 2013; pp. 73–119.
43. Saeseaw, S.; Renfro, D.N.; Palke, C.A.; Sun, Z.Y.; McClure, F.S. Geographic origin determination of emerald. *Gems Gemol.* **2019**, *55*, 614–646. [CrossRef]
44. Qin, L.J.; Yu, X.Y.; Guo, H.S. Fluid Inclusion and Chemical Composition Characteristics of Emeralds from Rajasthan Area, India. *Minerals* **2022**, *12*, 641. [CrossRef]
45. Platonov, A.N.; Taran, M.N.; Minko, O.E.; Polshyn, E.V. Optical absorption spectra and nature of color of iron-containing beryls. *Phys. Chem. Min.* **1978**, *3*, 87–88.
46. Spinolo, G.; Fontana, I.; Galli, A. Optical absorption spectra of Fe^{2+} and Fe^{3+} in beryl crystals Optical absorption spectra of Fe^{2+} and Fe^{3+} in beryl crystals. *Phys. Stat. Sol.* **2007**, *244*, 4660–4668. [CrossRef]
47. Schmetzer, K.; Berdesinski, W.; Bank, H. Über die Mineralart Beryll, ihre Farben und Absorptionsspektren. *Z. Dtsch. Gemmol. Ges.* **1974**, *23*, 5–39. (In German)
48. Adams, D.M.; Gardner, I.R. Single-crystal vibrational spectra of beryl and dioptase. *J. Chem. Soc.* **1974**, *14*, 1502–1505. [CrossRef]
49. Banerjee, A. Investigation of fluid inclusion in emeralds of different geological origins by microchemical analysis and IR-reflex ion-spectroscopy. *Boletín Soc. Española Mineral.* **1995**, *18*, 18–19.
50. Wood, D.L.; Nassau, K. Infrared spectra of foreign molecules in beryl. *J. Chem. Phys.* **1967**, *47*, 2220–2228. [CrossRef]
51. Wang, H.; Shu, T.; Chen, J.; Guo, Y. Characteristics of Channel-Water in Blue-Green Beryl and Its Influence on Colour. *Crystals* **2022**, *12*, 435. [CrossRef]
52. Bersani, D.; Azzi, G.; Lambruschi, E.; Barone, G.; Mazzoleni, P.; Raneri, S.; Longobardo, U.; Lottici, P.P. Characterization of emeralds by micro-Raman spectroscopy. *J. Raman Spectrosc.* **2014**, *45*, 1293–1300. [CrossRef]
53. Kim, C.C.; Bell, M.I.; McKeown, D.A. Vibrational analysis of beryl ($Be_3Al_2Si_6O_{18}$) and its constituent ring (Si_6O_{18}). *Phys. B. Condens.* **1995**, *205*, 193–208. [CrossRef]
54. Hagemann, H.; Lucken, A.; Bill, H.; Gysler-Sanz, J.; Stalder, H.A. Polarized Raman spectra of beryl and bazzite. *Phys. Chem. Min.* **1990**, *17*, 395–400. [CrossRef]
55. Huong, L.T.T.; Hager, T.; Hofmeister, W. Confocal micro-Raman spectroscopy: A powerful tool to identify natural and synthetic emeralds. *Gems Gemol.* **2010**, *46*, 139–148. [CrossRef]
56. Carey, D.M.; Korenowski, G.M. Measurement of the Raman spectrum of liquid water. *J. Chem. Phys.* **1998**, *108*, 2669–2675. [CrossRef]

Disclaimer/Publisher's Note: The statements, opinions and data contained in all publications are solely those of the individual author(s) and contributor(s) and not of MDPI and/or the editor(s). MDPI and/or the editor(s) disclaim responsibility for any injury to people or property resulting from any ideas, methods, instructions or products referred to in the content.